2019-01-0990 Published 02 Apr 2019

Sensitivity Study on Thermal and Soot Oxidation Dynamics of Gasoline Particulate Filters

Aki Takahashi, Slava Korneev, and Simona Onori Stanford University

Citation: Takahashi, A., Korneev, S., and Onori, S., "Sensitivity Study on Thermal and Soot Oxidation Dynamics of Gasoline Particulate Filters," SAE Technical Paper 2019-01-0990, 2019, doi:10.4271/2019-01-0990.

Abstract

Gasoline particulate filters (GPFs) are devices used to filter soot emitted by gasoline direct injection (GDI) engines.

A numerical model for a ceria-coated GPF presented in a previous paper by *H. Arunachalam et al. in 2017* was developed to predict internal temperature and soot amount combusted during regeneration events. Being that both the internal temperature and the accumulated soot cannot be directly measured during real-time operation and owing to their critical importance for GPF health monitoring as well as regeneration scheduling, the above model turns out to be a valuable tool for OBD applications. In this paper, we first conduct a stochastic analysis to understand the relation between the model parameters and the initial value of the ceria (IV) oxide volume fraction, as a deterministic value for such a state is not known. A particle swarm optimization (PSO) algorithm was employed to define what type of relationship the model parameters were with respect to the initial state of the ceria (IV) oxide volume fraction. A sensitivity study is then conducted over the model parameters to study parameter identifiability from system measurements. Effects of the initial temperature and initial amount of soot were studied as well. Results indicated that the model is most sensitive to the activation energy of GPF regeneration, agreeing with previous studies. Additionally, the model was shown to be able to predict the GPF temperature with less than 5% error when there was at most 20% uncertainty in the parameters. The results of the relationship between ceria (IV) oxide and the parameters, as well as the sensitivity analysis can be used simultaneously in the future for observer-based design.

Keywords

gasoline particulate filter, particle swarm optimization, sensitivity analysis, root mean square error

1. Introduction

Carbon based energy resources have become essential in many nations due to the increased usage of gasoline and diesel automobiles with consequent environmental concerns due to increased emissions of pollutants [1]. Development for high efficiency, environmentally friendly engines is therefore necessary for their viability in the modern world.

The gasoline direct injection (GDI) engine has been gaining more attention over the port fuel injection (PFI) engine due to the GDI engine's multiple benefits. In GDI engines fuel is directly sprayed into the combustion chamber, whereas in PFI engines fuel and air are mixed prior to combustion. The reduced probability of engine knocking, due to charge cooling from in-cylinder evaporation of fuel, allows for higher compression ratios [2]. As a result, GDI engines have higher fuel economy, greater power output, and lower carbon dioxide emissions than PFI engines [3]. However, GDI engines also have higher particulate matter (PM) emissions than PFI engines due to shorter air/fuel mixing times, fuel impingement onto the piston, and incomplete combustion inside the chamber [3,4]. PM mainly consists of soot particles, which are made of carbon and are carcinogenic [5]. Thus, various regulations in the EU, China, and other nations have been introduced to prevent excessive emissions of particulate matter [6]. Newer, more accurate emissions tests have also been installed to closely monitor PM in automobiles [7]. A separate technology is introduced to limit PM emissions. Gasoline particulate filters (GPFs) are the most promising solution to address the particulate emissions problem from GDI engines.

A wall-flow GPF consists of a monolithic structure with a bundle of axial parallel channels, that are alternatively plugged at each end so exhaust gas in the inlet channels is forced to flow across the porous walls of the GPF, as shown in Fig.1. Particulate is trapped inside the walls, and the exhaust gas leaves the GPF with significantly less PM. GPFs are based off diesel particulate filters (DPFs), which are technologies used to trap particulate from diesel engines [8]. DPFs and GPFs both have the same monolithic structure with parallel channels. While many studies have been conducted on the two filters and it was found there are overlapping aspects, it

FIGURE 1 Schematic of GPF. The exhaust gas enters the filter from the left and it passes through the filter leaving or trapping the particulate inside.

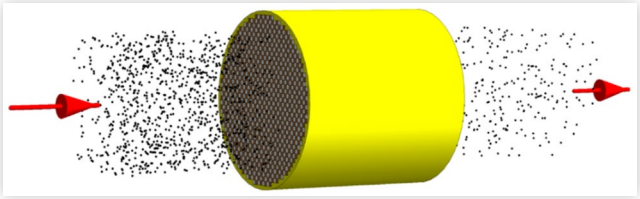

is important to distinguish the two technologies due to their unique operating conditions [2].

In DPFs, soot is initially trapped in the filter pores which determines the rapid rise in pressure drop. As the DPF continues to accumulate soot, a layer, which is more porous, is built on top of it - and called depth filtration - and pressure drop increases less rapidly and in a linear fashion. GPFs perform and behave slightly different from DPFs, due to the differences between gasoline and diesel exhaust [9]. For example, due to the lower soot emissions from GDI engines compared to diesel engines, there is much less soot being accumulated in the GPF [10]. Relative to the diesel operating environment, gasoline applications are generally characterized by hotter exhaust temperatures, stoichiometric (rather than lean) combustion, lower PM and smaller particles [11].

Given the differences in the operating environment and exhaust characteristics, GPFs and DPFs will differ in porosity, mean pore size, pore size distribution, and cell geometry [11]. Thus, in GPFs the formation of bed filtration can result only under very high soot loading. In normal operating GPF conditions, characterized by low soot loading, no depth filtration is formed in a GPF. Hence, given that the particle concentration is smaller and the exhaust is hotter, the depth filtration effect never develops in GPFs.

To avoid overtime accumulation of soot in the filter, with consequent buildup of backpressure in the exhaust system and loss of engine efficiency, GPFs must undergo periodic soot regeneration events to maintain the optimal regime for the engine. Regeneration, which consists in the oxidization of soot, requires high temperature and enough oxygen be present in the filter to initiate the combustion reaction [10]. DPFs operate optimally with active regeneration, where combustion is caused by an outside energy source. The DPF cannot passively regenerate, where combustion is caused by high temperatures of the gas exhaust, since the DPF operates with low gas exhaust temperature [12]. GPFs, on the other hand, operate at a higher gas exhaust temperature, so passive regeneration is mainly used for PM combustion [9]. Higher temperature consequently creates higher pressure drop due to the greater flow rate of PM and raises potential concerns of the GPF reaching critical temperatures before melting and limiting filtration efficiency [9].

It is, then, important to be able to know the GPF temperature and the amount of soot oxidized through various regeneration events to maximize engine efficiency. However, these quantities cannot be measured during real-time vehicle operation. Numerical models can instead be employed to accurately predict such values. In [13], the dynamics of temperature and soot oxidation for a ceria-coated GPF using a 0-D model were modeled and experimentally validated.

The physics-based model from [13], consisting in a set of nonlinear ordinary differential equations (ODEs) is a readily useful tool for the estimation of state variables that cannot be measured during real-time operation. This model though relies on parameters which are identified, from experimental data, only within a given accuracy. The uncertainty inside the parameters may lead to uncertainty to the estimation of the state variables. In order to understand the dependence of the model output performance on its identified parameters a sensitivity study is proposed in this paper. In particular, a sensitivity study of the thermal and soot oxidation dynamics inside a ceria-coated GPF was conducted on the activation energy and pre-exponential factors of the oxidation reaction and ceria catalysis. The lack of experimental data for the ceria volume fraction also called for a study of its effects on the the aforementioned parameters.

The paper is structured as follows: Section 2 summarizes the model and the experimental data collected in [13]. These are used for the sensitivity study. Section 3 discusses the sensitivity of the parameters to the initial ceria (IV) oxide volume fraction. Section 4 summarizes the main procedure and results of the sensitivity study.

2. GPF Mechanisms and Numerical Model

The 0-D model of soot oxidation used in this paper captures the dynamics of a coated GPF device. Measurements used for model development and validation were conducted over a GPF device that was placed downstream of a three-way catalytic converter (TWC) in a GDI engine-based vehicle. The purpose of the TWC is to prevent NOx, CO gases and HC from leaving the automobile by converting them into less harmful compounds such as NO_2, H_2O, and CO_2.

The numerical model developed in [13] is used in this study.

There are three main reactions that are considered in the model and take place inside the porous walls of the GPF during the regeneration process. Those are:

$$C + O_2 \rightarrow CO_2$$

$$2Ce_2O_3 + O_2 \rightarrow 4CeO_2 \quad (1)$$

$$C + 4CeO_2 \rightarrow 2Ce_2O_3 + CO_2$$

The reactions that include carbon monoxide as either reactant or product are not accounted for, since the concentration of carbon monoxide is found negligibly small at any time [13]. The applied reaction kinetics model is from [14]. The ceria reactions catalyze soot oxidation rates, therefore the

ceria-coating on the GPF increases the filtration efficiency of the GPF.

The input to state (output) block diagram of the GPF model exploited in this work is shown in Fig. 2, where the input vector is given by:

$$u = \left[T_{inlet}, \lambda_{pre,GPF}, \dot{m}_g \right] \tag{2}$$

The model is given by a set of ODEs with an algebraic equation consisting of multiple Arrhenius-type terms. The internal temperature of the GPF, the mass of the soot, and the concentration of ceria are predicted across time by the following equations [13]:

$$\frac{dT_{GPF}}{dt} = \frac{\dot{m}_g \cdot C_{p,gas}}{m_{GPF} \cdot C_{p,cord}} \cdot \left(T_{inlet} - T_{GPF} \right) + \frac{1}{m_{GPF} \cdot C_{p,cord}} \dot{Q}_{Reac} \tag{3}$$

$$\frac{dm_{c,GPF}}{dt} = -A_T \cdot \exp\left(-\frac{E_a^T}{RT_{GPF}} \right) \cdot m_{c,GPF} \cdot Y_{O_2} - A_{C,1} \cdot \exp\left(-\frac{E_a^{C,1}}{RT_{GPF}} \right) \cdot m_{c,GPF} \cdot Y_{CeO_2} \tag{4}$$

$$\frac{dY_{CeO_2}}{dt} = -A_{C,1} \cdot \exp\left(-\frac{E_a^{C,1}}{RT_{GPF}} \right) \cdot \frac{m_{c,GPF}}{m_{c,GPF,ini}} \cdot Y_{CeO_2} + A_{C,2} \cdot \exp\left(-\frac{E_a^{C,2}}{RT_{GPF}} \right) \cdot Y_{O_2} \cdot \left(1 - Y_{CeO_2} \right) \tag{5}$$

$$\dot{Q}_{Reac} = -\Delta H_T \cdot A_T \cdot \exp\left(-\frac{E_a^T}{RT_{GPF}} \right) \cdot \frac{m_{c,GPF}}{M_C} \cdot Y_{O_2} - \Delta H_{C,1} \cdot A_{C,1} \cdot \exp\left(-\frac{E_a^{C,1}}{RT_{GPF}} \right) \cdot \frac{m_{c,GPF}}{M_C} \cdot Y_{CeO_2} - \Delta H_{C,2} \cdot A_{C,2} \cdot \exp\left(-\frac{E_a^{C,2}}{RT_{GPF}} \right) \cdot \frac{\rho_{O_2} Y_{O_2} V_{exh}}{M_{O_2}} \cdot \left(1 - Y_{CeO_2} \right) \tag{6}$$

FIGURE 2 Input/state representation of the GPF model. The model inputs are inlet GPF temperature, T_{inlet}, the mass flow rate, $\dot{m}_g$, and the pre-GPF air-flow ratio, $\lambda_{pre,GPF}$. The states of the model are the mass of soot inside GPF, $m_{c,GPF}$, and the internal temperature of GPF, T_{GPF} and the oxygen volume fraction Y_{CeO2}.

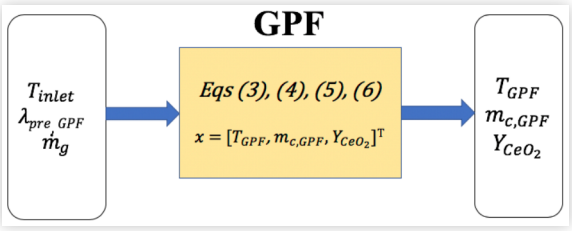

TABLE 1 Condition of operations, in terms of $T_{GPF,ini}$ and $m_{c,GPF,ini}$ for the three experiments conducted to calibrate the 0-D model. Initial soot amount decreases through each consecutive experiment, while $T_{GPF,ini}$ increases.

Experiment Name	*TGPF,ini* [K]	*mc,GPF,ini* [kg]
Regen 1	942.85	$9.34 \cdot 10^{-4}$
Tipout 1	954.89	$6.277 \cdot 10^{-4}$
Tipout 2	995.84	$4.605 \cdot 10^{-4}$

The parameter A_z is the pre-exponential factor for the three reaction rate expressions, while E_a^z is the activation energy for the three reactions, where z = T, C, 1 *or* C, 2 correspond to the reactions for soot combustion, ceria (IV) oxide regeneration, and ceria trioxide production, respectively. Other symbols are explained in the Nomenclature section.

Each reaction in Eq. 1 is associated with 2 unique parameters within the ODE model, for a total of 6 parameters considered. The parameter vector, θ, includes parameters that relate to each reaction rate, namely:

$$\theta = \left[A_T, A_{C,1}, A_{C,2}, E_a^T, E_a^{C,1}, E_a^{C,2} \right] \tag{7}$$

Note that E_a^T was set to be 149 [kJ/mol] for the GPF modeling based on previous studies [13]. The remaining parameters were calculated using the Particle Swarm Optimization (PSO) algorithm and experimental data collected during the three regeneration events shown in Table 1. A combined cost function of error in the thermal and soot oxidation dynamics was used to increase the reliability of the parameters [13]. The average GPF internal temperature, T_{avg}, and the experimental soot amount, $m_{c,exp}$, were used to optimize the model with respect to the experimental data within the lumped-parameter modeling approach used in [13].

The duration of each experiment was 80 seconds. The first event is denoted as Regen 1, while the second and last events are denoted Tipout 1 and Tipout 2, respectively. In the next sections, only analytical results found using Regen 1 experimental data are shown, since the state variables across the three experimental patterns displayed no patterns that distinguished one another when they were modeled.

Table 1 shows the initial values for the inlet temperature and initial soot mass, $T_{GPF,ini}$ and $m_{c,GPF,ini}$, respectively, for the three regeneration events. $T_{GPF,ini}$ increases across the regeneration events due to the decrease in soot amount. However, this increase in initial temperature is roughly 5.62% from Regen 1 to Tipout 2, thus it was concluded that the change was not significant enough for separate analysis in this paper. The initial ceria volume fraction, $Y_{CeO2,\,ini}$, on the other hand, is not known during any experiment since it is the product of an exothermic reaction [15]. $Y_{CeO2,\,ini}$ was therefore assumed to be 1 for all experiments in [13].

Fig. 3 shows how the states evolve subjected to the Regen 1 inputs, compared to the experimental data.

FIGURE 3 Results of the ODE model based on the parameter and initial condition values from [13] for the Regen 1 experimental data, compared with the experimental data. $Y_{CeO2,\,ini}$ is 1.

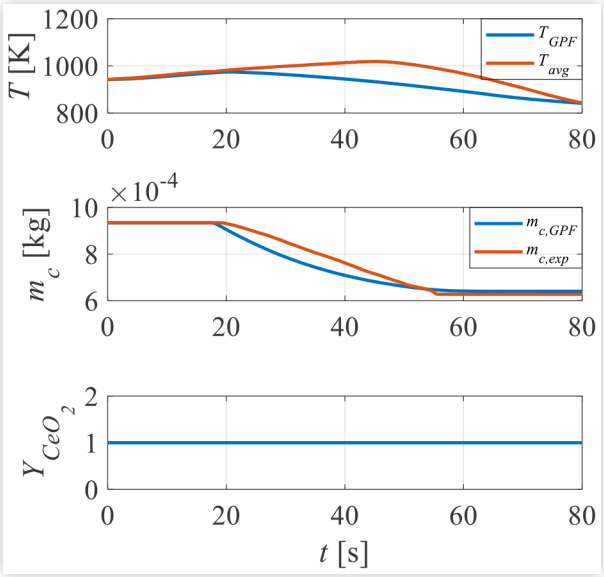

TABLE 2 List of the parameter identification options used in the PSO algorithm.

Option	Value/Setting
options.PopulationSize	1000
options.MaxIter	3000
options.TolFun	0.5×10^{-6}
options.StallGenLimit	250

TABLE 3 List of the identified parameters and their numerical initial ranges considered in the PSO-based identification.

Parameter	Range
A_T	$[1 \times 10^2, 1 \times 10^9]$
$A_{C,1}$	$[1, 1 \times 10^7]$
$A_{C,2}$	$[0.1, 1 \times 10^7]$
$E_a^{C,1}$	$[1 \times 10^3, 999 \times 10^3]$
$E_a^{C,2}$	$[1 \times 10^3, 999 \times 10^3]$

3. Consistency of Model with Initial CeO_2 Volume Fraction

There is not a well defined way to determine the initial value of the CeO_2 volume fraction due to the lack of experimental data, yet, CeO_2 has a significant impact on the reaction rates and other state variables during real-time operation due to its catalytic role. Parameters in [13] were identified under the assumption that $Y_{CeO2,\,ini}$ was equal to 1, which might not be the case. Fig. 3 illustrates that when $Y_{CeO2,\,ini}$ is 1, Y_{CeO2} does not evolve across time, which might not represent the actual behavior. Thus, to determine appropriate values for $Y_{CeO2,\,ini}$ and to address the relationship between $Y_{CeO2,\,ini}$ and the parameters, $Y_{CeO2,\,ini}$ is treated as a stochastic variable uniformly distributed between 0 and 1. Thus, by letting $Y_{CeO2,\,ini}$ vary between its admissible values, [0 1], we perform a new identification of the parameters using PSO for each admissible initial value of $Y_{CeO2,\,ini}$ within that range. Precisely, 101 evenly spaced values of $Y_{CeO2,\,ini}$ were tested, and the corresponding values of the model parameters were calculated with the PSO algorithm. Results are plotted in terms of their histogram distribution and scattered plots.

Table 2 summarizes the settings used for parameter identification. The PSO algorithm was set to terminate after 3000 iterations or if the generation did not improve after 250 iterations. The parameter ranges in Table 3 are not modified from [13], except for $A_{C,2}$ which was given a smaller lower bound due to previous sensitivity studies that indicated the parameter was consistently reaching the lower bound for varying $Y_{CeO2,\,ini}$ amounts.

If the probability density function of each of the parameters were a Gaussian curve, we would conclude that $Y_{CeO2,\,ini}$ had no effect on the parameters of the model and the mean values of the Gaussian curves could be taken as a numerical value of the parameter irrespective to the initial state $Y_{CeO2,\,ini}$.

Fig. 4 shows the histograms and scatterplots of the 5 parameters that were calculated by PSO with regards to the uniformly distributed $Y_{CeO2,\,ini}$ values on the range [0 1].

The results indicate that $E_a^{C,2}$ is independent of $Y_{CeO2,\,ini}$. The histogram is unimodal, and 98% of $E_a^{C,2}$ values are between $(0, 1{\cdot}10^5]$. There is very little variability, with 97% of values at exactly 1000 1/s. On the other hand, while the histogram and scatterplot for $A_{C,2}$ appear to show independence, Fig. 5 illustrates that it is dependent on $Y_{CeO2,\,ini}$ and increases nonlinearly between the range $(4.4{\cdot}10^{-1}, 5.2{\cdot}10^{-1})$ when not considering the outliers. This is consistent with the catalytic role of CeO_2 inside of the GPF, as it suggests that increasing the amount of CeO_2 also increases the rate of catalysis.

Similarly, A_T shows consistent increases between the range $(5{\cdot}10^6, 9{\cdot}10^6)$ as $Y_{CeO2,\,ini}$ increases, albeit the growth is not linear, barring the outlier is disregarded. This suggests that when there is a greater initial amount of CeO_2 the reaction rate of combustion is higher. This increase is also consistent with the catalytic role of CeO_2 inside the GPF.

The rest of the parameters show a random dependence on $Y_{CeO2,\,ini}$. Since none of the histograms in Fig. 4 shows a normal distribution, a Gaussian distribution in the probability density functions will not be observed either. This means that parameters excluding $E_a^{C,2}$ and E_a^T cannot be fully identified. For the sensivity analysis in Section 4 an arbirtray parameter set and $Y_{CeO2,\,ini}$ were thus selected.

However, the parameters that are dependent on $Y_{CeO2,\,ini}$ can be determined by a dedicated algorithm. This is beyond the scope of this paper.

FIGURE 4 Histograms and scatterplots of the model parameters with varying $Y_{CeO2,\,ini}$ uniformly in the range [0, 1].

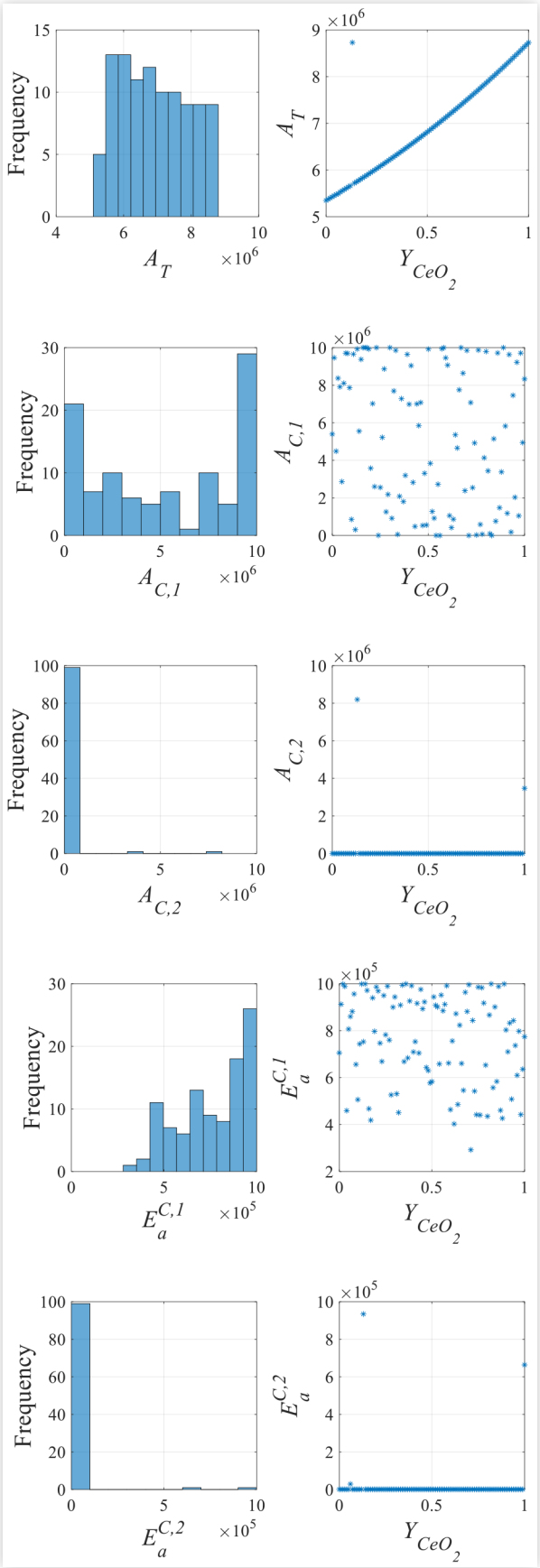

FIGURE 5 Histogram and scatterplot of $A_{C,2}$ without considering the outliers for varying $Y_{CeO2,\,ini}$ uniformly in the range [0, 1].

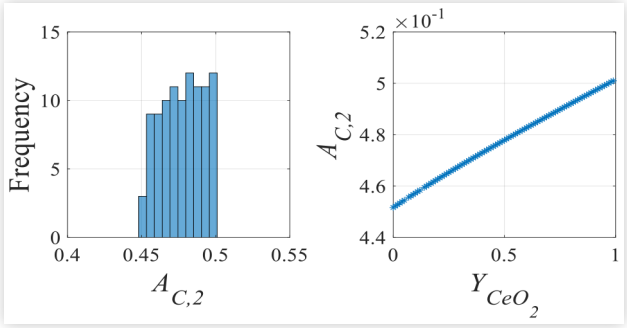

4. Sensitivity Study on Thermal and Oxidation Dynamics

For the sensitivity study conducted in this section, $Y_{CeO2,\,ini}$ is arbitrarily chosen to be 0.3. This value was concluded to be fit as an initial condition, as all parameters identified using a $Y_{CeO2,\,ini}$ value of 0.3 were within the modes of the parameter histograms shown in Fig.4. This suggests the parameter values identified with $Y_{CeO2,\,ini}$ set to 0.3 were more likely to occur than other possible values. The parameter values used as a baseline values for the sensitivity analysis are shown in Table 4.

The GPF model sensitivity study was conducted by calculating the effects of the parameters on the state variables.

Defining the state vector:

$$x_{GPF} = \left[x_1, x_2\ x_3\right] = \left[T_{GPF}, m_{c,GPF}, Y_{CeO_2}\right] \tag{8}$$

and the input vector:

$$\boldsymbol{u} = \left[u_1, u_2, u_3\right] \tag{9}$$

the numerical 0-D GPF model can be rewritten in the following state space representation:

$$\dot{x} = \boldsymbol{f}\left(\boldsymbol{x}, \boldsymbol{u}, t\right) \tag{10}$$

$$\boldsymbol{f} = \left[f_1,\ f_2, f_3\right] \tag{11}$$

$$\dot{x}_1 = \frac{u_3 \cdot C_{p,gas}\left(u_1, u_2\right)}{m_{GPF} \cdot C_{p,cord}} \cdot \left(u_1 - x_1\right) + \frac{1}{m_{GPF} \cdot C_{p,cord}} \cdot \dot{Q}_{Reac}$$

TABLE 4 The identified parameter values that were used in the sensitivity analysis of the ODE model. All values lie within the modes of their respective histograms in fig. 4.

Parameter	Identified Value
A_T	6.18×10^6
$A_{C,1}$	1.00×10^7
$A_{C,2}$	4.68×10^{-1}
$E_a^{C,1}$	9.435×10^5
$E_a^{C,2}$	1000

$$= f_1\left(x_1,x_2,x_3,u_1,u_2,u_3,t\right) \tag{12}$$

$$\dot{x}_2 = -A_T \cdot \exp\left(-\frac{E_a^T}{Rx_1}\right)\cdot x_2 \cdot Y_{O_2}\left(u_2\right)$$

$$- A_{C,1} \cdot \exp\left(-\frac{E_a^{C,1}}{Rx_1}\right)\cdot x_2 \cdot x_3$$

$$= f_2\left(x_1,x_2,x_{3,}\, u_{2,}\, t\right) \tag{13}$$

$$\dot{x}_3 = -A_{C,1} \cdot \exp\left(-\frac{E_a^{C,1}}{Rx_1}\right)\cdot \frac{x_2}{x_2(1)} \cdot x_3$$

$$+A_{C,2} \cdot \exp\left(-\frac{E_a^{C,2}}{Rx_1}\right)\cdot Y_{O_2}\left(u_2\right)\cdot\left(1-x_3\right)$$

$$= f_3\left(x_1,x_2,x_{3,}\, u_{2,}\, t\right) \tag{14}$$

$$\dot{Q}_{Reac} = -\Delta H_T \cdot A_T \cdot \exp\left(-\frac{E_a^T}{Rx_1}\right)\cdot \frac{x_2}{M_C}\cdot Y_{O_2}\left(u_2\right)$$

$$- \Delta H_{C,1} \cdot A_{C,1} \cdot \exp\left(-\frac{E_a^{C,1}}{Rx_1}\right)\cdot \frac{x_2}{M_C}\cdot x_3$$

$$- \Delta H_{C,2} \cdot A_{C,2} \cdot \exp\left(-\frac{E_a^{C,2}}{Rx_1}\right)\cdot \frac{\rho_{O_2 Y_{O_2} V_{exh}}}{M_{O_2}}\cdot\left(1-x_3\right) \tag{15}$$

The state-space representation of Eq. 11, 12, and 13 can be rewritten in such a way the state vector depends on the parameters. The parameters are cast into the vector θ:

$$\theta = \left[\theta_1,\theta_2,\theta_3,\theta_4,\theta_5,\theta_6\right] \tag{16}$$

Additionally, initial conditions of the states are also considered for the sensitivity study due to their potential influence on the model performance. In particular, the vector of initial conditions used for the sensitivity study is given by θ_0:

$$\theta_0 = \left[T_{GPF,ini}, m_{c,GPF,ini}\right] = \left[x_{1,0}, x_{2,0}\right] \tag{17}$$

The influence of $Y_{CeO2,\,ini}$ is illustrated in Fig. 4 and was explained in the previous section.

The full parameter and initial condition set used for our study is then:

$$\bar{\theta} = \left[\theta,\theta_0\right] \tag{18}$$

The state space representation of Eq. 12, 13, and 14, Eq. 10 becomes:

$$\dot{x} = \boldsymbol{f}\left(\boldsymbol{x},\boldsymbol{u},\bar{\boldsymbol{\theta}},\boldsymbol{t}\right) \tag{19}$$

Although there are 3 states predicted by the ODE model, the GPF temperature is the main concern for this study. The cordierite composing the GPF has a melting point of 1470° C [16]. To prevent the GPF from any possibility of melting however, the absolute GPF maximum temperature will be limited to less than 90% of the cordierite melting point, equivalent to 1568 K. The analytical studies were conducted by expressing the influence of each component in $\bar{\theta}$ on Eq. 12, 13, and 14. In the form of an expression, the effects are expressed by the partial derivatives of the state variables as follows:

$$\left.\frac{\partial x_1}{\partial \bar{\theta}_i}\right|_{\bar{\theta}_{j\neq i=const.}} \tag{20}$$

$$\left.\frac{\partial x_2}{\partial \bar{\theta}_i}\right|_{\bar{\theta}_{j\neq i=const.}} \tag{21}$$

$$\left.\frac{\partial x_3}{\partial \bar{\theta}_i}\right|_{\bar{\theta}_{j\neq i=const.}} \tag{22}$$

Eqs 20-22 indicate that only one component within $\bar{\theta}$ is changed at a time during the sensitivity study. Cross sensitivity between components in $\bar{\theta}$ was not considered due to the main concern of finding the effects of each parameter's uncertainty on the state variables.

Sensitivity analysis of the thermal dynamics is conducted by employing two different cost functions. The relative error cost function, *RE* compares the difference between the maximum of the nominal GPF temperature, $T_{GPF,\,nom}$, and the GPF temperature function with the varying parameter, $T_{GPF,\,var}$:

$$RE = \frac{max\left(T_{GPF,var}\right) - max\left(T_{GPF,nom}\right)}{max\left(T_{GPF,nom}\right)}\cdot 100 \tag{23}$$

The one exception to *RE* is when the initial GPF temperature exceeds the maximum GPF temperature after the regeneration event begins. For the sensitivity analysis of the initial GPF temperature, the relative error function's time domain is limited such that the lower boundary will not exceed the local maximum of the GPF temperature graph.

The RMS error formula $RMSE_{xi}$ compares the RMS error between the general nominal state function, $x_{GPF,\,nom}$, and the state function with varying $\bar{\theta}$, $x_{GPF,\,var}$. As an equation, $RMSE_{xi}$ is:

$$RMSE_{x_i} = \frac{\sqrt{\frac{1}{N}\cdot\sum_{t=1}^{N}\left(x_{GPF,var,\bar{\theta}i}(t) - x_{GPF,nom,}(t)\right)^2}}{mean\left(T_{GPF\,nom}\right)}\cdot 100 \tag{24}$$

Where N is the total number of time samples, t is the actual time and i is either the internal GPF temperature or soot amount state variable in vector x.

The parameters and initial conditions were altered by up to ±20% of their original values. The initial temperature will only be observed on the range of 0 to +20%; decreasing the initial temperature is not considered as it raises potential concerns for soot combustion failure during real-time operation. The range of changes in $\bar{\theta}$ was limited due to the sheer amount of possibilities for the parameters.

Fig. 6 shows results of Eq. 23 and 24 with regards to the changes in individual parameters and initial conditions in $\bar{\theta}$. Results illustrate that the ODE model is most sensitive to E_a^T. This is consistent with past studies that found E_a^T to greatly affect GPF temperature [17]. The analysis showed that two of the ceria parameters, namely $A_{C,\,1}$ and $E_a^{C,1}$, have no influence on the model output. These parameters are involved in the exothermic reaction to produce CeO_2, which does not require soot to take place. This means the reaction rate of CeO_2

FIGURE 6 Sensitivity analysis results across changes in parameters and initial conditions. The second RE plot is a magnified version of the original RE plot, as effects may not clear in the original RE plot. For the GPF temperature, its sensitivity to $x_{1,0}$ is only observed for increases in the initial condition.

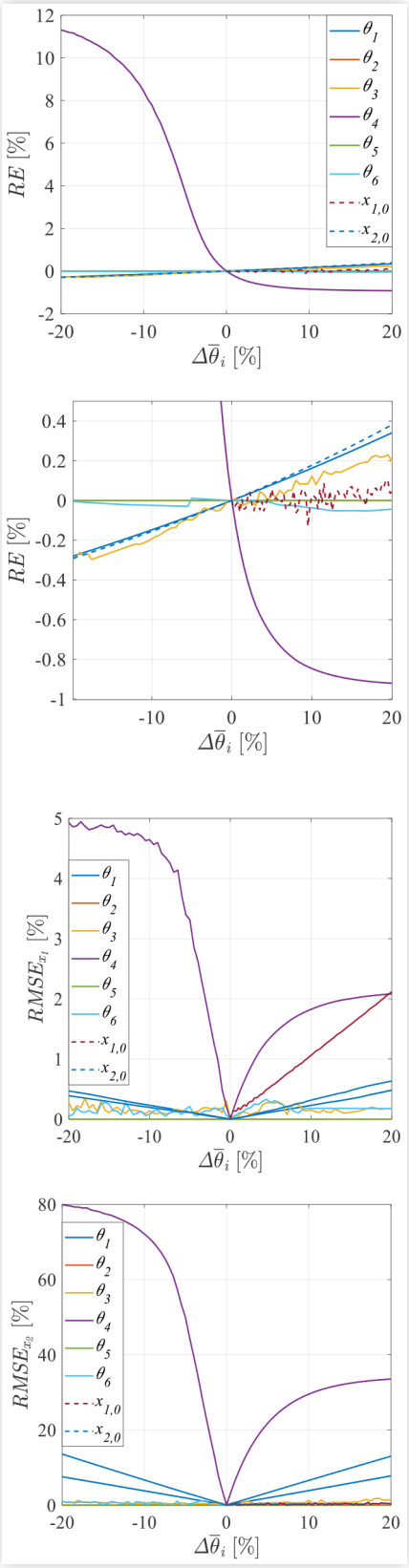

FIGURE 7 A plot of the T_{GPF} curve with various $T_{GPF,ini}$ across the experimental 80 second interval.

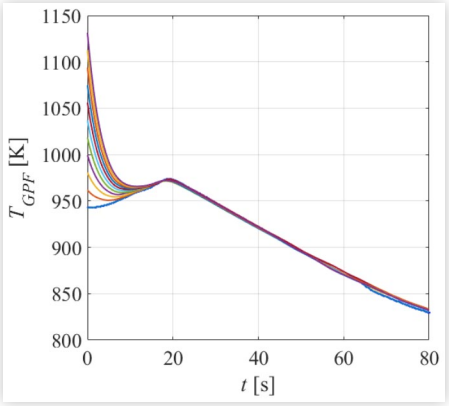

converting into Ce_2O_3 has no influence on both the internal GPF temperature and the soot amount. From a model structure standpoint, the lack of sensitivity of model output on those model parameters is an indication of lack of identifiability of those parameters. This may also explain the random dependence that $Y_{CeO2,\,ini}$ showed with respect to the two ceria parameters, which was observed in Fig. 4.

$T_{GPF,ini}$ seems to have conflicting results between the RMSE and RE graphs, since the maximum GPF temperature changes by a degree less than 1% for all changes in the initial condition, yet the RMSE consistently grows. This phenomenon is likely due to the increasing distance between the nominal and varying $T_{GPF,ini}$. Fig. 7 shows multiple curves for the predicted T_{GPF} with various $T_{GPF,ini}$ values across the entire 80 second interval. It is evident that all of the curves quickly converge despite having varied initial GPF temperatures. Thus the GPF temperature state's sensitivity to $T_{GPF,ini}$ is not significant. Other parameters caused less than 0.8% RMS error in T_{GPF}, indicating within this 20% range, the parameters and initial condition of the state variables have a relatively low effect on the accuracy of the ODE model.

None of the parameters caused the GPF temperature to exceed the 90% temperature boundary. We can therefore conclude that within 20% error of likely parameter values in real-time operation, the GPF has a very low risk of melting.

On the other hand, The soot amount state variable is far more sensitive to changes in many of the parameters. Aside from the influence of E_a^T, both the RMS error caused by changes in A_T and $m_{c,\,GPF,\,ini}$ were found to linearly increase to reach about 8% and 13% RMS error at the maximum uncertainty, respectively. The soot amount was not as sensitive to the remaining parameters with RMS error remaining below 2%.

5. Conclusions

This paper presents the results of a sensitivity analysis on the thermal and oxidation dynamics of the ODE model developed in [13]. The sensitivity analysis was conducted by observing the individual effects of the parameters and initial conditions

on the model output. The relative error of the maximum GPF temperature, as well as the total RMSE of the thermal and soot oxidation models were considered for the analysis. Results showed that the thermal and oxidation dynamics were particularly sensitive to E_a^T. The initial GPF temperature has no influence on the thermal dynamics, as any changes are quickly negated by the quick convergence to the nominal thermal function. None of the parameters caused the GPF temperature to exceed the temperature limitation, thus there is very little risk of the GPF melting during regeneration. Additionally, within 20% error of the identified parameters, the model can accurately predict the GPF temperature with less than 5% error. The soot amount, on the other hand, is moderately sensitive to multiple parameters. Soot amount should be closely monitored during real-time operation to prevent over- or underestimation of the current soot amount with this model.

Influence of $Y_{CeO2,\,ini}$ values on the overall model parameters was also investigated. The analysis showed that reactions related to the catalysis of soot were not affected by changes in $Y_{CeO2,\,ini}$, whereas the regeneration of the catalytic layer showed random dependence. This is likely due to the unidentifiability of the CeO_2 parameters.

Both results will help observability during real-time operation of the GPF in automobiles. The algorithm to determine the relation between $Y_{CeO2,\,ini}$ and the parameters is the next step for this ODE model. Furthermore, additional experiments and measurements will be needed to legitimize the identifiability of the parameters with respect to the volume fraction of the catalyst. This will ultimately allow the model to be applicable for future observer-based design.

6. Acknowledgements

The authors are grateful to Dr. Harikesh Arunachalam for his insights and guidelines about the 0-D GPF model. This work is supported by the National Science Foundation under grant No. CAREER CMMI 1839050.

References

1. Cao, L. et al., "Importance of Carbon Dioxide Physiological Forcing to Future Climate Change," *Proceedings of the National Academy of Sciences*, 2010.
2. Joshi, A. and Johnson, T.V., "Gasoline Particulate Filters-A Review," *Emission Control Science and Technology* 4:4, 219-239, 2018.
3. Zhu, R., Hu, J., Bao, X., He, L. et al., "Tailpipe Emissions from Gasoline Direct Injection (GDI) and Port Fuel Injection (PFI) Vehicles at Both Low and High Ambient Temperatures," *Environmental Pollution* 216:223-234, 2016.
4. Karjalainen, P., Pirjola, L., Heikkila, J., Lahde, T. et al., "Exhaust Particles of Modern Gasoline Vehicles: A Laboratory and an On-Road Study," *Atmospheric Environment* 97:262-270, 2014.
5. United States, Environmental Protection Agency, "Health and Environmental Effects of Particulate Matter (PM)," 2018.
6. Weiss, M. et al., "Will Euro 6 reduce the NOx emissions of new diesel cars?-Insights from on-road tests with Portable Emissions Measurement Systems (PEMS)," *Atmospheric Environment* 62:657-665, 2012.
7. Merkisz, J., Pielecha, J., Bielaczyc, P., and Woodburn, J., "Analysis of Emission Factors in RDE Tests as Well as in NEDC and WLTC Chassis Dynamometer Tests," SAE Technical Paper 2016-01-0980, 2016, doi:10.4271/2016-01-0980.
8. Cutler, W.A. and Hickman, D.L., "Diesel Particulate Filters," U.S. Patent No. 6,464,744, Oct. 15, 2002.
9. Saito, C., Nakatani, T., Miyairi, Y., Yuuki, K. et al., "New Particulate Filter Concept to Reduce Particle Number Emissions," SAE Technical Paper 2011-01-0814, 2011, doi:10.4271/2011-01-0814.
10. Chan, T., Meloche, E., Kubsh, J., Rosenblatt, D. et al., "Evaluation of a Gasoline Particulate Filter to Reduce Particle Emissions from a Gasoline Direct Injection Vehicle," *SAE Int. J. Fuels Lubr.* 5(3):1277-1290, 2012, doi:10.4271/2012-01-1727.
11. Sappok, A., Wang, Y., Wang, R., Kamp, C. et al., "Theoretical and Experimental Analysis of Ash Accumulation and Mobility in Ceramic Exhaust Particulate Filters and Potential for Improved Ash Management," *SAE Int. J. Fuels Lubr.* 7(2):511-524, 2014, doi:10.4271/2014-01-1517.
12. Görsmann, C., "Catalytic Coatings for Active and Passive Diesel Particulate Filter Regeneration," *Monatshefte für Chemie/Chemical Monthly* 136:1, 91-105, 2005.
13. Arunachalam, H., Pozzato, G., Hoffman, M.A., and Onori, S., "Modeling the Thermal Dynamics Inside a Ceria-Coated Gasoline Particulate Filter," in *2017 IEEE Conference on Control Technology and Applications (CCTA)*, Mauna Lani, HI, 2017, 99-105.
14. Pozzato, G., Hoffman, M., and Onori, S., "Multi-Channel Physics-Based Modeling and Experimental Validation of an Uncoated Gasoline Particulate Filter in Clean Operating Conditions," in *2017 American Control Conference*, Seattle, WA, May 24-26, 2017.
15. Lide, D.R. and Haynes, W.M., *CRC Handbook of Chemistry and Physics: A Ready-Reference Book of Chemical and Physical Data* (Boca Raton, FL: CRC, 2009).
16. Rohan, P. et al., "Thermal and Mechanical Properties of Cordierite, Mullite and Steatite Produced by Plasma Spraying," *Ceramics International* 30:4, 597-603, 2004.
17. Boger, T. et al., "Oxidation of Soot (Printex® U) in Particulate Filters Operated on Gasoline Engines," *Emission Control Science and Technology* 1:1, 49-63, 2015.

Nomenclature

$\Delta \boldsymbol{H_T}$ - soot combustion enthalpy, -393.5 $\cdot 10^3$ [J/mol]

$\Delta \boldsymbol{H_{C,1}}$ - ceria trioxide production reaction enthalpy, 368.90 $\cdot 10^3$ [J/mol]

$\Delta \boldsymbol{H_{C,2}}$ - ceria regeneration reaction enthalpy, -762.4 $\cdot 10^3$ [J/mol]

$\boldsymbol{\lambda_{pre,GPF}}$ - pre-GPF air-flow ratio [-]

$\boldsymbol{\rho_{cord}}$ - density of cordierite, 1100 [kg/m^3]

$\boldsymbol{\rho_{O2}}$ - density of oxygen, [kg/m^3]

$\boldsymbol{A_T}$ - pre-exponential factor for the standard combustion reaction, [1/s]

$\boldsymbol{A_{C,1}}$ - pre-exponential factor for the ceria trioxide production reaction, [1/s]

$\boldsymbol{A_{C,2}}$ - pre-exponential factor for the ceria regeneration reaction, [1/s]

$\boldsymbol{C_{p,cord}}$ - specific heat capacity of the cordierite, 1173.3 [$J/(kgK)$]

$\boldsymbol{C_{p,gas}}$ - specific heat capacity of the gas exhaust, [$J/(kgK)$]

$\boldsymbol{E_a^T}$ - soot combustion reaction activation energy, [J/mol]

$\boldsymbol{E_a^{C,1}}$ - ceria trioxide production reaction activation energy, [J/mol]

$\boldsymbol{E_a^{C,2}}$ - ceria regeneration reaction activation energy, [J/mol]

$\boldsymbol{m_{c,exp}}$ - mass of soot determined experimentally, [kg]

$\boldsymbol{m_{c,GPF}}$ - predicted mass of soot, [kg]

$\boldsymbol{m_{c,GPF,ini}}$ - initial mass of soot prior to regeneration, [kg]

$\boldsymbol{\dot{m}_g}$ - measured exhaust gas mass flow rate, [kg/s]

$\boldsymbol{m_{GPF}}$ - total mass of cordierite in the coated GPF, found by product of ρ_{cord} and V_{cord} [kg]

$\boldsymbol{M_C}$ - carbon molar mass, $12 \cdot 10^{-3}$ [kg/mol]

$\boldsymbol{M_{O2}}$ - carbon dioxide molar mass, $44 \cdot 10^{-3}$ [kg/mol]

$\boldsymbol{\dot{Q}_{Reac}}$ - net heat rate of the regeneration reactions, [J/s]

$\boldsymbol{R}$ - ideal gas constant, 8.314 [J/(molK)]

$\boldsymbol{RE}$ - relative error, [%]

$\boldsymbol{RMSE}$ - root mean square error, [%]

$\boldsymbol{t}$ - time [s]

$\boldsymbol{T_{ave}}$ - experimentally determined average temperature of the GPF, [K]

$\boldsymbol{T_{GPF}}$ - predicted temperature of the GPF, [K]

$\boldsymbol{T_{GPF,ini}}$ - initial GPF temperature, [K]

$\boldsymbol{T_{inlet}}$ - measured exhaust gas temperature at the inlet of the GPF, [K]

$\boldsymbol{V_{cord}}$ - total volume of cordierite in the GPF, $0.1828 \cdot 10^{-3}$ [m^3]

$\boldsymbol{V_{exh}}$ - filter trapping volume, $1.222 \cdot 10^{-3}$ [m^3]

$\boldsymbol{Y_{CeO2}}$ - volume fraction of ceria, [–]

$\boldsymbol{Y_{CeO2,ini}}$ - Initial volume fraction of ceria, [–]

$\boldsymbol{Y_{O2}}$ - volume fraction of oxygen, [–]

ISSN 0148-7191